A Cross-Decoupled Current Harmonics Suppression Method for IPMSM Based on Notch Filter and Second-Order Generalized Integrator

Chao Du, *Member, IEEE*, Shuang Yang, Lin Qiu, *Senior Member, IEEE*, Jien Ma, *Member, IEEE*, Youtong Fang, *Senior Member, IEEE*, and Jose Rodriguez, *Life Fellow, IEEE*

***Abstract*—The second-order generalized integrator (SOGI) is widely applied for current harmonics suppression of interior permanent magnet synchronous motors (IPMSMs). However, SOGI is single-degree of freedom and exists a tradeoff issue between the dynamic convergence response and the stable convergence precision. Thus, the final performance of current harmonics suppression is influenced. In order to address this issue, a cross-decoupled current harmonics suppression method based on notch filter and SOGI (NF-SOGI) is proposed. First, according to the opposite characteristics of SOGI and NF, SOGI is applied to extract the target current harmonic, while NF is applied to extract all the nontarget current harmonics, and thus, the target current harmonic is decoupled with the nontarget ones. Second, through the cross-link between SOGI and NF, NF-SOGI is reconstructed as double-degree of freedom, and there are two coefficients to cope with the tradeoff issue, and thus, the convergence precision can be improved under the same convergence rate. Therefore, the suppression performance of current harmonics is enhanced. Finally, the effectiveness of the proposed scheme is validated on a 17.26-kW IPMSM drive platform.**

***Index Terms*—Current harmonics suppression, interior permanent magnet synchronous motors (IPMSMs), notch filter (NF), second-order generalized integrator (SOGI).**

I. Introduction

INTERIOR permanent magnet synchronous motors (IPMSM) have been widely used in industrial applications and household electrical appliances. It has various advantages such as high power density, high efficiency, good speed regulation performance, and compact structure [1], [2]. In recent years, IPMSM control system has been strictly required in the application of high-precision and high-efficiency fields [3]. However, the inverter of IPMSM control system has nonlinear characteristics caused by dead time and voltage drop, which introduce the time harmonics into the closed current loop of PMSM [4], [5]. Meanwhile, the flux spatial harmonics caused by cogging effect and magnetic saturation effect are also introduced into the closed current loop of PMSM [6], [7], [8]. The above two kinds of current harmonics lead to torque ripple, vibration, and noise during the motor operation, which reduce the stability of IPMSM control system and strictly restrict the application of IPMSM in high-precision fields [9], [10], [11], [12], [13]. Therefore, in order to extend the motor life, improve the torque quality, and reduce additional energy loss, it is necessary to suppress the current harmonics in the closed loop control of PMSM.

The recently researches on current harmonics suppression methods can be divided into two categories. As for the flux spatial harmonics, the related suppression methods are mainly applied to optimize the motor design, such as the stator shape optimization, the windings distribution modification, and the installation position adjustment of permanent magnets, the influence of cogging effect and magnetic saturation effect on stator current can be reduced. As for the time harmonics, the related suppression methods are mainly applied to optimize the control schemes. The dead-time and voltage drop are regarded as disturbances and observed through extended state observer, and the disturbances are eliminated by nonlinear proportional-integral-derivative (PID) controller [14], [15], [16]. The most widely suppression method is based on harmonics voltage injection [17], [18], [19], [20] and adaptive filter [21], [22], [23]. In [21], aiming at the first and second harmonics caused by the current sensor measurement, the harmonics are eliminated through the adaptive-frequency harmonic suppression strategy based on the vector reconstruction. In [22], in order to reduce the torque ripples caused by harmonic currents, the harmonic currents are estimated through adaptive filter and eliminated through harmonic current controller. In [23], account for non-sinusoidal back electromotive force, the current harmonics are suppressed by a self-tuning compensation voltage through an

Received 16 August 2024; revised 17 October 2024; accepted 15 November 2024. Date of publication 29 November 2024; date of current version 28 January 2025. This work was supported in part by the National Key Research and Development Program of China under Grant 2022YFB4201600, in part by China Postdoctoral Science Foundation Research Fund under Grant 2022M712931 and Grant 2023T160603, in part by Key Research and Development Plan of Zhejiang Province under Grant 2023C01243, and in part by State Key Laboratory of Fluid Power and Mechatronic Systems under Grant SKLoFP_ZZ_2302. Recommended for publication by Associate Editor H. Chaoui. *(Corresponding author: Lin Qiu.)*

Chao Du and Shuang Yang are with the College of Electrical and Control Engineering, Shaanxi University of Science and Technology, Xi'an 710021, China (e-mail: duchao@sust.edu.cn; 220611007@sust.edu.cn).

Lin Qiu, Jien Ma, and Youtong Fang are with the College of Electrical Engineering, Zhejiang University, Hangzhou 310058, China (e-mail: qiu_lin@zju.edu.cn; majien@zju.edu.cn; youtong@zju.edu.cn).

Jose Rodriguez is with the Universidad San Sebastián, Santiago 8420524, Chile (e-mail: jose.rodriguezp@uss.cl).

Color versions of one or more figures in this article are available at https://doi.org/10.1109/TPEL.2024.3507939.

Digital Object Identifier 10.1109/TPEL.2024.3507939

adaptive linear neuron. In these current harmonics suppression methods above, they have a good suppression effect on current harmonics. However, the observer is constructed with complex mathematical model, the repeated coordinate transformations increase the calculation amount of the system, and the adaptive filters applied in the current harmonics extraction exists the tradeoff issue because of the step size μ. At present, second-order generalized integrator (SOGI) is gifted with simple mathematic model and it has been widely applied in power grid and motor control [24], [25], [26], [27], [28], [29], [30], [31]. In [24], SOGI is applied to estimate the accurate parameters of grid voltage under unbalanced and distorted grid conditions. In [25], a fast estimation method of voltage harmonics is introduced into frequency locked loop based on SOGI, and the proposed method can achieve high levels of power quality. In [26], a cascade multiple SOGIs are used to extract the first-order and second-order harmonics caused by offset error and scaling error. In [30], SOGI is adopted to extract the current harmonics in IPMSM sensor-less drives system, in order to eliminate the error in the position estimation. In [31], a flux estimation method based on SOGI is proposed without the phase lag and amplitude attenuation at the resonant frequency, and the shortcomings of flux observer based on low-pass filter are overcome. However, the performance of SOGI are closely associated with the internal factor and the external factor. As the internal factor, traditional SOGI has only proportionality coefficient m, which is a tradeoff between the convergence rate and the convergence precision, so that SOGI is single-degree of freedom, and the dynamic convergence response and the stable convergence precision cannot be improved at the same time. Meanwhile, as the external factor, the target current harmonic is coupled with the nontarget current harmonics in SOGI, which deteriorates the convergence precision of target current harmonic. Therefore, the tradeoff issue and the coupled issue affect the final suppression performance of current harmonics.

In order to address the tradeoff issue and the coupled issue, a cross-decoupled current harmonics suppression method based on notch filter and SOGI (NF-SOGI) is proposed in this article. In NF-SOGI, utilizing the opposite characteristics of SOGI and NF in the same central frequency, SOGI is applied to extract the target current harmonic, while NF is applied to extract the nontarget current harmonics, and thus, the target current harmonic is decoupled with the nontarget ones in NF-SOGI. Through the cross-link between SOGI and NF, the proposed NF-SOGI is reconstructed as double-degree of freedom. In details, there are two proportionality coefficients to cope with the tradeoff issue of parameter, the proportionality coefficient m is firstly set to guarantee the dynamic convergence, and then the proportionality coefficient k improves the stable convergence precision. Thus, both dynamic convergence rate and stable convergence precision can be adjusted at the same time. Therefore, more precise target current harmonic can be rapidly convergent, so that the suppression performance of target current harmonics is enhanced and verified by the stator current waveforms and fast Fourier transformation (FFT) analysis of stator current in the closed current loop.

The rest of this article is organized as follows. In Section II, the current harmonics model of IPMSM is established. In Section III, the principles of SOGI is introduced, and the current harmonics suppression based on SOGI is analyzed. In Section IV, a cross-decoupled current harmonics suppression method based on NF-SOGI is proposed, the convergence performance of current harmonics is verified through bode diagrams and simulation, and the stability is analyzed through Nyquist criterion, and the parameters design is discussed based on the amplitude-frequency response. In Section V, the proposed method is verified by experimental results. Finally, Section VI concludes this article.

II. Current Harmonics Model of IPMSM

IPMSM control system is a complex system because of its nonlinear, multivariable, and strongly coupled characteristics. The mathematical model of IPMSM can be transformed to d-q synchronous rotating coordinate frame to facilitate the model analysis. In this article, IPMSM is considered as an ideal structure, hence, flux linkage harmonics can be neglected. The voltage equations of IPMSM are shown in

$$\begin{cases} u_d = R_s i_d + L_d \frac{di_d}{dt} - \omega L_q i_q \\ u_q = R_s i_q + L_q \frac{di_q}{dt} + \omega L_d i_d + \omega \psi_f \end{cases} \tag{1}$$

where u_d and u_q are d-axis and q-axis components of stator voltage, respectively; i_d and i_q are d-axis and q-axis components of stator current, respectively; L_d and L_q are d-axis and q-axis components of stator inductance, respectively; R_s is stator resistance; ω is electric angular velocity; ψ_f is flux linkage of permanent magnets.

The stator windings of IPMSM are mainly connected with star connection in the actual motor control system, and the windings are distributed symmetrically in the ideal condition. Therefore, there is no $3n$-order ($n = 1, 3, 5 \ldots$) and even-order stator current harmonics, and the phase difference between stator current harmonics is $2n\pi/3$. The current harmonics can be expressed in

$$\begin{cases} i_{an} = i_{n\text{th}} \cos(n\omega t + \theta_n) \\ i_{bn} = i_{n\text{th}} \cos(n\omega t - \frac{2}{3}\pi + \theta_n) \\ i_{cn} = i_{n\text{th}} \cos(n\omega t + \frac{2}{3}\pi + \theta_n) \end{cases} \tag{2}$$

where i_{an}, i_{bn} and i_{cn} are n-order stator current harmonics of a-phase, b-phase and c-phase, respectively; i_{nth} is the amplitude of n-order stator current harmonic; θ_n is the initial phase of n-order stator current harmonic.

In (2), the stator current harmonics are (6n$\pm$1)-order ($n = 1, 2, 3 \ldots$), and the content of stator current harmonics are decreased with the increase order of current harmonics, so that low-order stator current harmonics have much more content than high-order stator current harmonics. Thus, the main stator current harmonics are 5th, 7th, 11th, and 13th stator current harmonics, and they are considered as the suppression target, so that the stator current of IPMSM including 5th, 7th, 11th, and 13th stator

current harmonics can be expressed in

$$\begin{cases} i_a = i_{1\text{th}}\cos(\omega t+\theta_1)+i_{5\text{th}}\cos(5\omega t+\theta_5) \\ \quad +i_{7\text{th}}\cos(7\omega t+\theta_7)+i_{11\text{th}}\cos(11\omega t+\theta_{11}) \\ \quad +i_{13\text{th}}\cos(13\omega t+\theta_{13}) \\ i_b = i_{1\text{th}}\cos(\omega t+\theta_1-\frac{2\pi}{3})+i_{5\text{th}}\cos(5\omega t+\theta_5-\frac{2\pi}{3}) \\ \quad +i_{7\text{th}}\cos(7\omega t+\theta_7-\frac{2\pi}{3})+i_{11\text{th}}\cos(11\omega t+\theta_{11}-\frac{2\pi}{3}) \\ \quad +i_{13\text{th}}\cos(13\omega t+\theta_{13}-\frac{2\pi}{3}) \\ i_c = i_{1\text{th}}\cos(\omega t+\theta_1+\frac{2\pi}{3})+i_{5\text{th}}\cos(5\omega t+\theta_5+\frac{2\pi}{3}) \\ \quad +i_{7\text{th}}\cos(7\omega t+\theta_7+\frac{2\pi}{3})+i_{11\text{th}}\cos(11\omega t+\theta_{11}+\frac{2\pi}{3}) \\ \quad +i_{13\text{th}}\cos(13\omega t+\theta_{13}+\frac{2\pi}{3}) \end{cases} \tag{3}$$

where $i_{1\text{th}}$, $i_{5\text{th}}$, $i_{7\text{th}}$, $i_{11\text{th}}$, and $i_{13\text{th}}$ are amplitude of fundamental current, 5th, 7th, 11th, and 13th stator current harmonics, respectively; θ_1, θ_5, θ_7, θ_{11}, and θ_{13} are initial phase angle of fundamental current, 5th, 7th, 11th, and 13th stator current harmonics, respectively.

Under the constraint condition of constant amplitude, the stator currents in (3) are transformed to d-q synchronous rotating coordinate frame in (4). Through the Clarke and Park transformation, 5th and 7th stator current harmonics in i_{abc} are transformed to sixth current harmonics in i_{dq}, and 11th and 13th stator current harmonics in i_{abc} are transformed to 12th current harmonics in i_{dq}. Except for dc components, 6th and 12th current harmonic have the most content in i_d and i_q, and cause the biggest damage to the motor performance among all the current harmonics. Therefore, 6th and 12th current harmonic are chosen as the suppression target. The current equations including 6th and 12th current harmonic are shown in

$$\begin{cases} i_d = i_{1\text{th}}\cos\theta_1+i_{5\text{th}}\cos(-6\omega t+\theta_5)+i_{7\text{th}}\cos(6\omega t+\theta_7) \\ \quad +i_{11\text{th}}\cos(-12\omega t+\theta_{11})+i_{13\text{th}}\cos(12\omega t+\theta_{13}) \\ i_q = i_{1\text{th}}\sin\theta_1+i_{5\text{th}}\sin(-6\omega t+\theta_5)+i_{7\text{th}}\sin(6\omega t+\theta_7) \\ \quad +i_{11\text{th}}\sin(-12\omega t+\theta_{11})+i_{13\text{th}}\sin(12\omega t+\theta_{13}). \end{cases} \tag{4}$$

Combine (4) into (1), the voltage equations including 6th and 12th current harmonic can be obtained in

$$\begin{cases} u_d = R_s i_{1\text{th}}\cos\theta_1-\omega L_q i_{1\text{th}}\sin\theta_1 \\ \quad +(6\omega L_d-\omega L_q)i_{5\text{th}}\sin(-6\omega t+\theta_5) \\ \quad +R_s i_{5\text{th}}\cos(-6\omega t+\theta_5) \\ \quad -(6\omega L_d+\omega L_q)i_{7\text{th}}\sin(6\omega t+\theta_7) \\ \quad +R_s i_{7\text{th}}\cos(6\omega t+\theta_7) \\ \quad +(12\omega L_d-\omega L_q)i_{11\text{th}}\sin(-12\omega t+\theta_{11}) \\ \quad +R_s i_{11\text{th}}\cos(-12\omega t+\theta_{11}) \\ \quad -(12\omega L_d+\omega L_q)i_{13\text{th}}\sin(12\omega t+\theta_{13}) \\ \quad +R_s i_{13\text{th}}\cos(12\omega t+\theta_{13}) \\ u_q = R_s i_{1\text{th}}\sin\theta_1+\omega L_d i_{1\text{th}}\cos\theta_1+\omega\psi_f \\ \quad -(6\omega L_q-\omega L_d)i_{5\text{th}}\cos(-6\omega t+\theta_5) \\ \quad +R_s i_{5\text{th}}\sin(-6\omega t+\theta_5) \\ \quad +(6\omega L_q+\omega L_d)i_{7\text{th}}\cos(6\omega t+\theta_7) \\ \quad +R_s i_{7\text{th}}\sin(6\omega t+\theta_7) \\ \quad -(12\omega L_q-\omega L_d)i_{11\text{th}}\cos(-12\omega t+\theta_{11}) \\ \quad +R_s i_{11\text{th}}\sin(-12\omega t+\theta_{11}) \\ \quad +(12\omega L_q+\omega L_d)i_{13\text{th}}\cos(12\omega t+\theta_{13}) \\ \quad +R_s i_{13\text{th}}\sin(12\omega t+\theta_{13}). \end{cases} \tag{5}$$

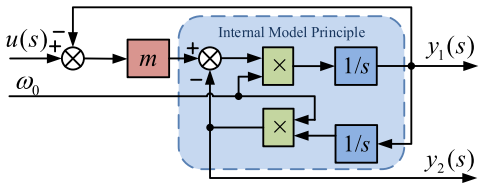

Fig. 1. Structure diagram of typical SOGI.

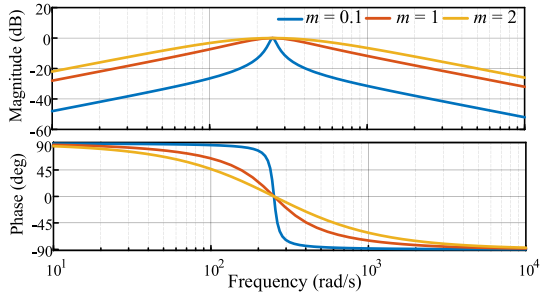

Fig. 2. Bode diagram of $G_{\text{SOGI\_BF}}(s)$.

III. Current Harmonics Suppression Method Based on SOGI

A. Principles of SOGI

Typical SOGI works as a signal processor, and it is used for signal extraction or filtration. The structure diagram of typical SOGI is shown in Fig. 1, where ω_0 is the resonant frequency and designed by the target frequency, m is the proportionality coefficient, $u(s)$ is the input signal, and $y_1(s)$ and $y_2(s)$ are the outputs of extraction and filtration, respectively. Through the different output channels, specific frequency signal is extracted or filtered, and the transfer functions of $y_1(s)/u(s)$ and $y_2(s)/u(s)$ are shown in (6) and (7), respectively, where $G_{\text{SOGI\_BF}}(s)$ and $G_{\text{SOGI\_LF}}(s)$ are the transfer function of the extraction channel and filtration channel, respectively, as follows:

$$G_{\text{SOGI\_BF}}(s)=\frac{y_1(s)}{u(s)}=\frac{m\omega_0 s}{s^2+m\omega_0 s+\omega_0^2} \tag{6}$$

$$G_{\text{SOGI\_LF}}(s)=\frac{y_2(s)}{u(s)}=\frac{m\omega_0^2}{s^2+m\omega_0 s+\omega_0^2}. \tag{7}$$

According to the internal model principle, in order to track a signal without static error, there must be a same dynamic model in the system. The Laplace transformation of sinusoidal signal is $s/(s^2+\omega^2)$, which is included in the transfer function of $G_{\text{SOGI\_BF}}(s)$. Thus, SOGI can track the target sinusoidal signal without static error. The bode diagrams of $G_{\text{SOGI\_BF}}(s)$ and $G_{\text{SOGI\_LF}}(s)$ are shown in Figs. 2 and 3, respectively, where the resonant frequency ω_0 is 80 π rad/s, m is selected as 0.1, 1, and 2. It can be concluded that $G_{\text{SOGI\_BF}}(s)$ and $G_{\text{SOGI\_LF}}(s)$ can be regarded as a band-pass filter and a low-pass filter, respectively.

In Fig. 2, it can be seen that the amplitude of resonant frequency ω_0 is reserved without phase shift, while the amplitude of all nonresonant frequency is attenuated with varying degrees, thereby the target signal with specific frequency is extracted.

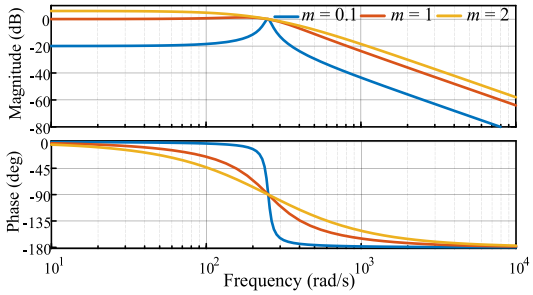

Fig. 3. Bode diagram of $G_{\mathrm{SOGI\_LF}}(s)$.

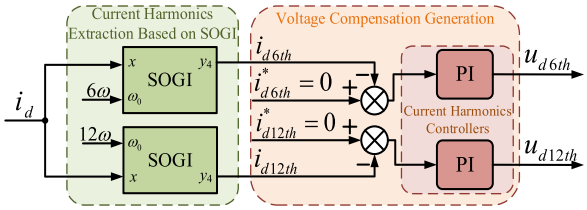

Fig. 4. Block diagram of current harmonics suppression method based on SOGI.

With the decrease of m, the bandwidth of band-pass filter is narrowed, and the attenuation effect on the nonresonant frequency is enhanced. It indicates that the stable convergence precision of SOGI gets better, but the dynamic convergence response of SOGI gets slower.

In Fig. 3, it can be seen that at the resonant frequency point, the gain is 0 dB and the phase lag is 90°. The proportionality coefficient m decides the filtering effect of high-frequency disturbances. With the decrease of m, the filtering effect of the high-frequency disturbances is enhanced, but the dynamic performance of SOGI is deteriorated.

B. Analysis on the Current Harmonics Suppression Based on SOGI

According to the analysis above, SOGI can work as a band-pass filter to obtain the target frequency signal without amplitude attenuation and phase shift. Therefore, SOGI is competent to extract 6th and 12th current harmonic. Take the d-axis for example, 6th and 12th current harmonic obtained from SOGI are subtracted with the command values, which are set to zero, and the voltage compensation values are generated through proportional-integral (PI) controllers. The block diagram of current harmonics suppression method based on SOGI is shown in Fig. 4, where $i^*_{d6\mathrm{th}}$ and $i^*_{d12\mathrm{th}}$ are the command values of current harmonics; $i_{d6\mathrm{th}}$ and $i_{d12\mathrm{th}}$ are the target 6th and 12th current harmonic from SOGI; $u_{d6\mathrm{th}}$ and $u_{d12\mathrm{th}}$ are the injected compensation voltage. The current harmonics suppression method mainly includes two parts: 1) current harmonics extraction and 2) voltage compensation generation.

The block diagram of current harmonics suppression method based on SOGI in IPMSM control system is shown in Fig. 5. Double closed-loop vector control structure is adopted, and PI controllers in the forward channel are applied for fundamental

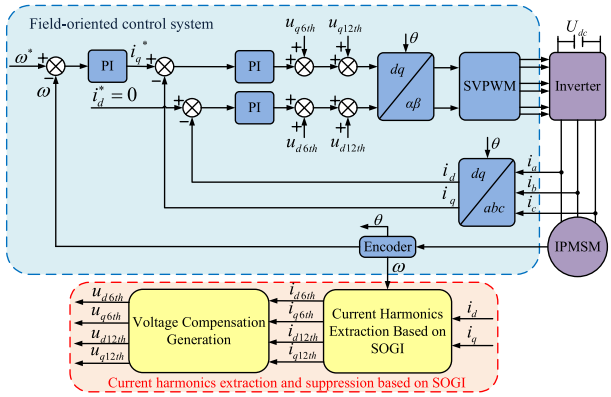

Fig. 5. Block diagram of current harmonics suppression method based on SOGI in IPMSM control system.

current control, while PI controllers in the suppression method are applied for 6th and 12th current harmonic suppression. The fundamental current controllers and the current harmonics controllers operate independently, so that 6th and 12th current harmonic are effectively suppressed while the fundamental current control is not affected. Finally, the compensation voltage is injected into the voltage control signal in the current loop. Therefore, in order to extend the motor life, improve the torque quality, and reduce additional energy loss, the current harmonics in the closed loop control of IPMSM is suppressed in this article.

Typical SOGI has only adjustment parameter m, which is a tradeoff between the convergence rate and the convergence precision, so that SOGI is single-degree of freedom, and thus, dynamic convergence response and stable convergence precision are always compromising considered. Meanwhile, the tradeoff issue results in the coupled relations among different order current harmonics. The stable convergence precision of target current harmonics is affected by nontarget current harmonics. Therefore, the tradeoff issue and the coupled issue affects the final suppression performance of current harmonics.

IV. Cross-Decoupled Current Harmonics Suppression Method Based on NF-SOGI

In order to solve the tradeoff issue and the coupled issue of SOGI, aiming at the improvement of current harmonics suppression effect, a cross-decoupled current harmonics suppression method based on notch filter and SOGI (NF-SOGI) is proposed in this article.

A. Cross-Decoupled NF-SOGI

In the proposed NF-SOGI, notch filter (NF) can rapidly attenuate the specific frequency signal at resonant frequency point, and then eliminates this signal. The structure diagram of NF is shown in Fig. 6, where ω_0 is the resonant frequency, $u(s)$ is the input signal, k is the filter coefficient and affects the bandwidth of NF, and $y_3(s)$ is the output signal. The transfer function $G_{\mathrm{NF}}(s)$ is obtained in

$$G_{\mathrm{NF}}(s) = \frac{y_3(s)}{u(s)} = \frac{s^2 + \omega_0^2}{s^2 + 2k\omega_0 s + \omega_0^2}. \tag{8}$$

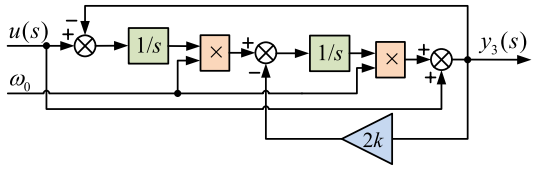

Fig. 6. Structure diagram of NF.

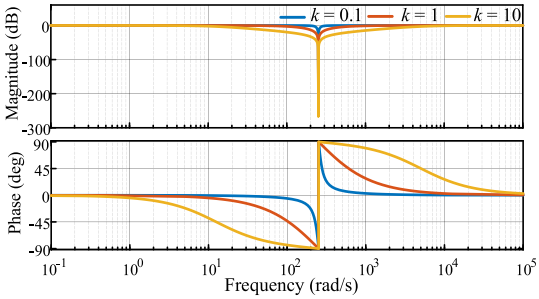

Fig. 7. Bode diagram of $G_{NF}(s)$.

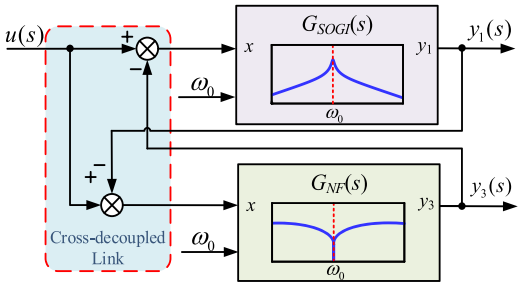

Fig. 8. Simplified structure diagram of the cross-decoupled NF-SOGI.

The bode diagram of $G_{\mathrm{NF}}(s)$ is shown in Fig. 7, where the resonant frequency ω_0 is 80 π rad/s, k is selected as 0.1, 1, and 10. It can be indicated that NF works as a band-stop filter, and a signal with the resonant frequency can be eliminated, while signals with nonresonant frequency are retained. With the decrease of k, the bandwidth of NF gets narrow, which brings a better elimination effect on resonant frequency.

Through the analysis on the bode diagrams of SOGI and NF (as shown in Figs. 2 and 7), it can be indicated that NF has the opposite characteristics with SOGI at resonant frequency point. SOGI works as a band-pass filter, while NF works as a band-stop filter. In details, SOGI reserves the signal at the resonant frequency point, while NF eliminates the signal at the resonant frequency point. Therefore, SOGI is applied to extract the target current harmonic, NF can be applied to extract all the nontarget current harmonics to realize the decoupled between the target current harmonic and the nontarget current harmonics. Therefore, NF is introduced into SOGI, and the simplified structure diagram of NF-SOGI is shown in Fig. 8, where ω_0 is the target frequency, $u(s)$ is the input signal, $y_1(s)$ is the target current harmonic, and $y_3(s)$ is the sum of all the nontarget current harmonics.

In the cross-decoupled NF-SOGI, first, according to opposite characteristics of SOGI and NF at the resonant frequency point,

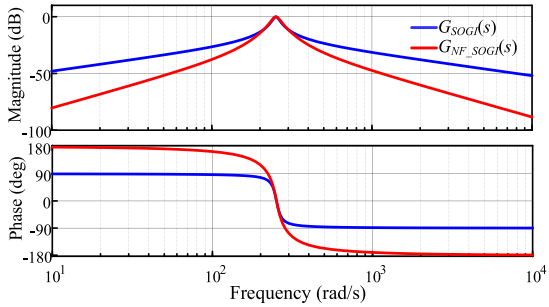

Fig. 9. Bode diagrams of $G_{\mathrm{SOGI}}(s)$ and $G_{\mathrm{NF\text{-}SOGI}}(s)$.

SOGI is applied to extract the specific target current harmonic, while NF is applied to extract all the nontarget current harmonics, so that the target current harmonic is decoupled with the nontarget current harmonics, and the convergence precision of target current harmonic is improved. Second, NF and SOGI are interactive connected in a cross-link structure, where the output of NF contributes to eliminate the nontarget current harmonics in the input of SOGI, and improve the attenuation of SOGI on the nontarget current harmonics, so that more precision target current harmonic is convergent through SOGI. Similarly, the nontarget current harmonics from NF are convergent more precisely because of SOGI. More precision convergence results can improve the convergence effect in the end. The transfer function of the cross-decoupled NF-SOGI is shown in (9). The bode diagram of typical SOGI and the proposed NF-SOGI are compared and shown in Fig. 9, where the resonant frequency ω_0 is 80 π rad/s

$$G_{\mathrm{NF-SOGI}}(s) = \frac{y_1(s)}{u(s)} = \frac{2km\omega_0^2 s^2}{s^4 + 2k\omega_0 s^3 + 2(km+1)\omega_0^2 s^2 + 2k\omega_0^3 s + \omega_0^4}. \quad (9)$$

Compared with the typical SOGI, the attenuation effect on the nontarget current harmonics is improved by the cross-decoupled NF-SOGI, so that the influence of the nontarget current harmonics on the target current harmonic is reduced, and the convergence precision of target current harmonic is enhanced, and thus the target and nontarget current harmonics are decoupled.

Through the bilinear transformation, the difference equations of NF-SOGI in discrete domain are obtained shown in (10) and (11), which are applied for the software programming in the experiment. Therefore, NF-SOGI can be realized in the software. In the cross-link structure, the input and output signals of NF and SOGI satisfies $X_{\mathrm{SOGI}}(k) = X_{\mathrm{SOGI}}(k\text{-}1)\text{-}Y_{\mathrm{NF}}(k\text{-}1)$, $X_{\mathrm{NF}}(k) = X_{\mathrm{NF}}(k\text{-}1)\text{-}Y_{\mathrm{SOGI}}(k\text{-}1)$ among different cycles. The current harmonics controllers and the fundamental current controller can operate independently, and thus the target 6th and 12th current harmonic are effectively suppressed while the fundamental current control is not affected

$$Y_{\mathrm{NF}}(k) = \frac{-(2\omega_0^2 T^2 - 8)}{(4 + 4k\omega_0 T + \omega_0^2 T^2)} Y_{\mathrm{NF}}(k-1)$$

$$+\frac{-(4-4k\omega_0T+\omega_0^2T^2)}{(4+4k\omega_0T+\omega_0^2T^2)}Y_{\mathrm{NF}}(k-2)+\frac{(4+\omega_0^2T^2)}{(4+4k\omega_0T+\omega_0^2T^2)}X_{\mathrm{NF}}(k)+\frac{(2\omega_0^2T^2-8)}{(4+4k\omega_0T+\omega_0^2T^2)}X_{\mathrm{NF}}(k-1)+\frac{(4+\omega_0^2T^2)}{(4+4k\omega_0T+\omega_0^2T^2)}X_{\mathrm{NF}}(k-2) \quad (10)$$

$$Y_{\mathrm{SOGI}}(k)=\frac{-(2\omega_0^2T^2-8)}{(4+2m\omega_0T+\omega_0^2T^2)}Y_{\mathrm{SOGI}}(k-1)+\frac{-(4-2m\omega_0T+\omega_0^2T^2)}{(4+2m\omega_0T+\omega_0^2T^2)}Y_{\mathrm{SOGI}}(k-2)+\frac{(2m\omega_0T)}{(4+2m\omega_0T+\omega_0^2T^2)}X_{\mathrm{SOGI}}(k)+\frac{(-2m\omega_0T)}{(4+2m\omega_0T+\omega_0^2T^2)}X_{\mathrm{SOGI}}(k-2). \quad (11)$$

B. Theoretical Analysis of Cross-Decoupled NF-SOGI

1) Analysis on Effectiveness: The time domain expression of total current harmonics can be uniformly expressed in (12), which contains the current harmonics with different frequencies

$$i(t)=\sum_{h=6n,n=1}^{\infty}A_h\sin(\omega_h t+\varphi_h) \quad (12)$$

where h is the order of each current harmonic; A_h is the amplitude of each current harmonic; ω_h is the frequency of each current harmonic. φ_h is the phase of each current harmonic. Through the Fourier transformation, the time domain expression can be transformed to the complex frequency domain in

$$I(s)=\sum_{h=6n,n=1}^{\infty}A_h\frac{s\sin\varphi_h+\omega_h\cos\varphi_h}{s^2+\omega_h^2}. \quad (13)$$

The main order of current harmonics in d-axis and q-axis are sixth, that is $h=6$. Focusing on the sixth current harmonic and the nonsixth current harmonics, the analysis on SOGI and NF-SOGI are discussed, respectively, and compared eventually.

As for target sixth current harmonic, ω_0 of SOGI is designed as 6ω, and $G_{\mathrm{SOGI}}(j6\omega)$ can be expressed in

$$G_{\mathrm{SOGI}}(j6\omega)=\frac{j6^2m\omega^2}{j6^2m\omega^2}=1\angle 0^\circ. \quad (14)$$

As for nonsixth current harmonics, $s=jh\omega$, h is the order of nonsixth current harmonics, $h=6n$. Bring $s=jh\omega$ into $G_{\mathrm{SOGI}}(s)$, $G_{\mathrm{SOGI}}(jh\omega)$ can be expressed in

$$G_{\mathrm{SOGI}}(jh\omega)=\frac{j6mh}{(6^2-h^2)+j6mh}. \quad (15)$$

Similarly, in NF-SOGI, the transfer function of $G_{\text{NF-SOGI}}(j6\omega)$ and $G_{\text{NF-SOGI}}(jh\omega)$ are expressed in

$$G_{\mathrm{NF-SOGI}}(j6\omega)=\frac{-6^4km\omega^4}{-6^4km\omega^4}=1\angle 0^\circ \quad (16)$$

$$G_{\mathrm{NF-SOGI}}(jh\omega)=\frac{72h^2km}{72h^2(km+1)-(6^4+h^4)+j(12kh^3-432kh)}. \quad (17)$$

According to (14)–(17), the theoretical analysis on SOGI and NF-SOGI can be concluded that the target sixth current harmonic is extracted without phase shift and amplitude attenuation, and the nonsixth current harmonics are attenuated with varying degrees. The conclusion is consistent with the analysis in Section III-A. However, the performance difference between SOGI and NF-SOGI is the different amplitude gains and phases of nonsixth current harmonics shown in (18), which is calculated from (15) and (17). The attenuation effect on the nonsixth current harmonics of SOGI is only determined by parameter m, and m is usually designed by quality factor, but it exists a tradeoff between the dynamic performance and the stable precision, while the attenuation effect on nonsixth current harmonics of cross-decoupled NF-SOGI is determined by parameter k and m instead

$$\begin{cases}|G_{\mathrm{SOGI}}(jh\omega)|=\frac{1}{\sqrt{1+\left(\frac{6^2-h^2}{6hm}\right)^2}}\\ |G_{\mathrm{NF-SOGI}}(jh\omega)|=\frac{1}{\sqrt{\left(\frac{72h^2(km+1)-(6^4+h^4)}{72h^2km}\right)^2+\left(\frac{6^2-h^2}{6hm}\right)^2}}\\ \angle G_{\mathrm{SOGI}}(jh\omega)=\angle\left(\frac{\pi}{2}-\arctan\frac{6mh}{6^2-h^2}\right)\\ \angle G_{\mathrm{NF-SOGI}}(jh\omega)=\angle\left(\frac{\pi}{2}-\arctan\frac{72h^2(km+1)-(6^4+h^4)}{12hk(6^2-h^2)}\right).\end{cases} \quad (18)$$

Under the premise of the same dynamic performance, in order to obtain a better attenuation effect on all the nonsixth current harmonics in NF-SOGI than that in SOGI, the limit condition can be restricted in

$$\left|\frac{72h^2(km+1)-(6^4+h^4)}{72h^2km}\right|>1\Rightarrow km<f(h)=\left(\frac{h^2-36}{12h}\right)^2,h>6 \quad (19)$$

where the upper bound value of km should be less than the minimum value of $f(h)$, and $f(h)_{\min}$ is 0.5625 when $h_{min}=12$, (cause $h=6$n, the orders of nonsixth current harmonics are 12, 18, 24 …). Thus, the limit range is obtained in (20), and regarding to most values of k and m, their multiplication satisfies this limit range. Therefore, the attenuation effect on the nonsixth current harmonics is better in NF-SOGI

$$0<km<0.5625,k\in(0,1),m\in(0,1). \quad (20)$$

In NF-SOGI, m can be set first to guarantee the dynamic convergence response of target current harmonic, and then the stable convergence precision of target current harmonic can be improved through k. Therefore, when the cross-decoupled NF-SOGI is applied for current harmonics suppression, m and k can be adjusted independently to achieve a better stable convergence precision with the same dynamic convergence response of SOGI.

In order to compare the convergence performance of target current harmonics between typical SOGI and cross-decoupled NF-SOGI, the input current signal $u(t)$ is designed in (21), and

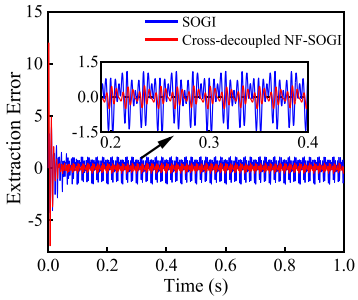

Fig. 10. Convergence error comparison between SOGI and NF-SOGI.

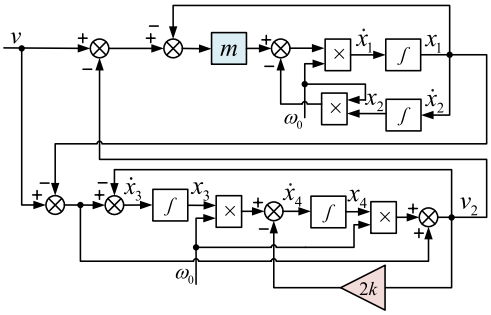

Fig. 11. Detailed structure diagram of the cross-decoupled NF-SOGI.

it is composed of current harmonics with different orders

$$u(t) = 100 + 5\sin(2\omega t) + 5\sin(3\omega t) + 15\sin(6\omega t) + 5\sin(9\omega t) + 10\sin(12\omega t) + 2\sin(18\omega t) \quad (21)$$

where the signal $15\sin(6\omega t)$ is a sixth current harmonic as the target. The resonant frequency of typical SOGI and cross-decoupled NF-SOGI is the same and designed as 6ω, and the convergence precision of target current harmonic is verified by the stable state error between the output and the reference $15\sin(6\omega t)$ in Fig. 10. It can be seen that the cross-decoupled method has a smaller stable state error, thereby the convergence precision of target current harmonics is better in NF-SOGI.

Benefits from the cross-decoupled design, the target current harmonic is decoupled with the nontarget current harmonics, the influence of nontarget current harmonics on the convergence precision of target current harmonic is decreased, more precision feedback value of target current harmonic is obtained. Moreover, more convergence precision of target current harmonic builds a better basis for the subsequent current harmonics suppression.

2) Analysis on Stability: The detailed structure diagram of NF-SOGI is shown in Fig. 11, and the state space formula of NF-SOGI is expressed in (22), where $\boldsymbol{x}$ is the state variables, $\boldsymbol{A}$ is the status matrix, $\boldsymbol{B}$ is the input matrix, and $\boldsymbol{v}$ is the input variables. It can be seen that both the dynamic response and stability of NF-SOGI depend on the values of m and k

$$\dot{\boldsymbol{x}} = \mathbf{A}\boldsymbol{x} + \mathbf{B}\boldsymbol{v}$$

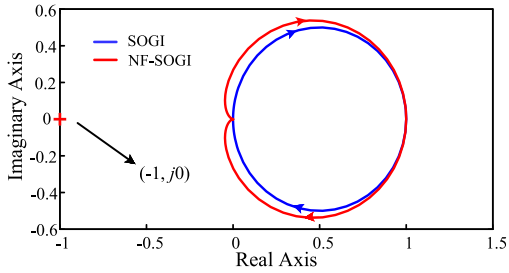

Fig. 12. Nyquist curves of SOGI and NF-SOGI.

$$\begin{bmatrix}\dot{x}_1\\ \dot{x}_2\\ \dot{x}_3\\ \dot{x}_4\end{bmatrix} = \begin{bmatrix}0 & -\omega_0^2 & 0 & -m\omega_0^2\\ 1 & 0 & 0 & 0\\ 0 & 0 & 0 & -\omega_0\\ 0 & 0 & \omega_0 & -2k\omega_0\end{bmatrix}\begin{bmatrix}x_1\\ x_2\\ x_3\\ x_4\end{bmatrix} + \begin{bmatrix}0\\ 0\\ 0\\ -2k\end{bmatrix} v. \quad (22)$$

Take the steady state operating conditions into account, that is $x_1 = v$, so that the actual input of NF is 0, and thus, the output of NF v_2 is also 0. The stable state space formula can be converted to (23), where $\bar{\boldsymbol{x}}$ represents the steady-state value of state variables

$$\dot{\bar{\boldsymbol{x}}} = \begin{bmatrix}\dot{\bar{x}}_1\\ \dot{\bar{x}}_2\\ \dot{\bar{x}}_3\\ \dot{\bar{x}}_4\end{bmatrix} = \begin{bmatrix}0 & -\omega_0^2 & 0 & 0\\ 1 & 0 & 0 & 0\\ 0 & 0 & 0 & -\omega_0\\ 0 & 0 & \omega_0 & 0\end{bmatrix}\begin{bmatrix}\bar{x}_1\\ \bar{x}_2\\ \bar{x}_3\\ \bar{x}_4\end{bmatrix}. \quad (23)$$

Through the characteristic determinant of Jacobian matrix, the eigenvalues are obtained in (24), where the Jacobian matrix represents as $\mathbf{J}$. It can be seen that both of eigenvalues have zero real part on the imaginary axis, and it indicates the oscillatory convergence characteristics of NF-SOGI, so that NF-SOGI maintains a convergent steady state response on the signal with frequency ω_0

$$|\lambda\mathbf{E} - \mathbf{J}| = \begin{vmatrix}\lambda & \omega_0^2 & 0 & 0\\ -1 & \lambda & 0 & 0\\ 0 & 0 & \lambda & \omega_0\\ 0 & 0 & -\omega_0 & \lambda\end{vmatrix} \Rightarrow \lambda_{1,2} = \pm j\omega_0. \quad (24)$$

The Nyquist curves of SOGI and the proposed NF-SOGI are shown in Fig. 12. According to the Nyquist stability criterion, the $(-1, j0)$ is not surrounded by the Nyquist curve of NF-SOGI, and when $L(\omega_0) > 0$, $(2k+1)\pi$ $(k = 0, \pm 1 \ldots)$ is not traversed by the phase-frequency characteristic curve. Therefore, the poles with positive real part are not included in the transfer function of NF-SOGI, and it indicates that NF-SOGI is stable in the variation range of ω_0.

3) Analysis on Response Time: The response time comparison between SOGI and NF-SOGI is analyzed by the settling time, which is obtained by the poles of characteristic equations. Through the closed-loop transfer function $G_{\mathrm{SOGI}}(s)$ and $G_{\mathrm{NF\_SOGI}}(s)$, the characteristic equations of SOGI and NF-SOGI are shown in (25) and (26), respectively. The root-locus of SOGI and cross-decoupled NF-SOGI are obtained in Figs. 13 and 14, where m is 0.5, k is 0.7, and the resonant frequency ω_0

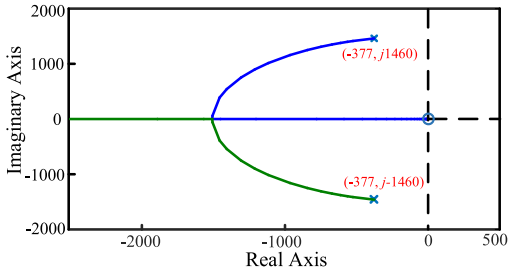

Fig. 13. Root-locus of SOGI.

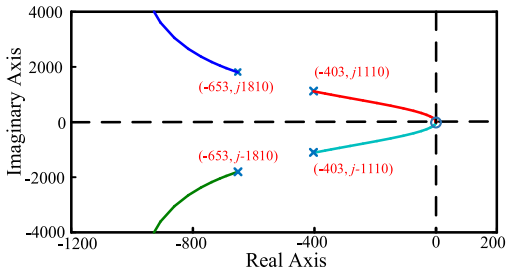

Fig. 14. Root-locus of NF-SOGI.

is $6 \times 80\ \pi$ rad/s

$$s^2 + m\omega_0 s + \omega_0^2 = 0 \tag{25}$$

$$s^4 + 2k\omega_0 s^3 + 2(km+1)\omega_0^2 s^2 + 2k\omega_0^3 s + \omega_0^4 = 0. \tag{26}$$

It can be seen that the real part of conjugate poles is -377 in the root-locus of SOGI, and the real part of two pairs of conjugate poles are -653 and -403 in the root-locus of NF-SOGI, respectively. There is no closed-loop zero around the poles closest to the imaginary axis. Based on the classical control theory, the real part of closed-loop poles plays a role in the response time. A smaller real part of closed-loop poles leads to a larger time constant of system, and thus, the dynamic response process is more slowly. The settling time T_s is usually defined when the steady state error e_{ss} is within 2%, and it is calculated by

$$T_s = \frac{4.4}{\sigma} \tag{27}$$

where σ is the absolute value of real part of the poles. As fourth-order system, NF-SOGI has two pairs of conjugate poles, whose position are very close, so that the nondominant poles cannot be ignored. Both the dominant poles and the nondominant poles have the effect on the dynamic response, and its approximate σ is the average of two real parts. Therefore, T_s of SOGI and cross-decoupled NF-SOGI can be calculated in

$$\begin{cases} T_{s\_\text{SOGI}} = \frac{4.4}{377} = 0.01176 \\ T_{s\_\text{NF-SOGI}} = \frac{4.4}{(653+403)/2} = 0.0083. \end{cases} \tag{28}$$

It can be concluded that NF-SOGI has a faster dynamic response than SOGI. Benefit from the design of parameter k, the real part absolute value of closed-loop poles in NF-SOGI is bigger than that in SOGI, and thus, the time constant of NF-SOGI is less than that of SOGI, so that the dynamic response process is faster in NF-SOGI.

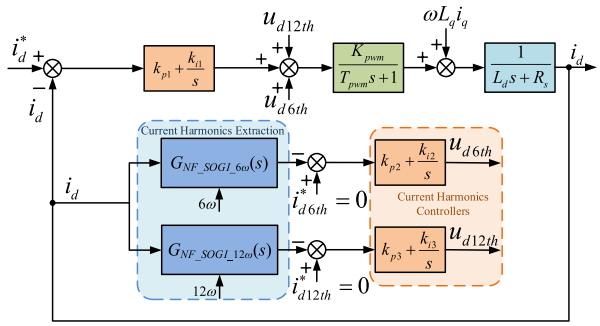

Fig. 15. Block diagram of d-aixs current harmonics suppression method based on cross-decoupled NF-SOGI.

C. Cross-Decoupled Current Harmonics Suppression Based on NF-SOGI

According to the analysis on the cross-decoupled NF-SOGI, more precise target current harmonics are obtained, thereby it contributes to improve the current harmonics suppression effect. The proposed cross-decoupled NF-SOGIs are applied to extract 6th and 12th current harmonic in i_d and i_q because of its faster convergence rate and higher convergence precision. Take the d-axis current loop for example, the d-axis current harmonics suppression method based on cross-decoupled NF-SOGI is shown in Fig. 15. Where, $G_{\text{NF-SOGI\_6}\omega}(s)$ and $G_{\text{NF-SOGI\_12}\omega}(s)$ are the transfer functions of 6th and 12th current harmonic suppression method based on cross-decoupled NF-SOGI, respectively; k_{p1} and k_{i1} are proportional coefficient and integral coefficient of PI controller in the d-axis current loop, respectively; k_{p2} and k_{i2} are proportional coefficient and integral coefficient of PI controller for sixth current harmonic control, respectively; k_{p3} and k_{i3} are proportional coefficient and integral coefficient of PI controller for 12th current harmonic control, respectively; K_{pwm} is the gain of the inverter; T_{pwm} is the switching period of the inverter.

The open loop transfer function of d-axis current loop with the current harmonic suppression method based on cross-decoupled NF-SOGI is (29) shown at the bottom of the next page, where $G_{\text{PI1}}(s)$ is the transfer function of PI controller in the d-axis current loop; $G_{\text{PI2}}(s)$ is the transfer function of PI controller for sixth current harmonic control; $G_{\text{PI3}}(s)$ is the transfer function of PI controller for 12th current harmonic control.

When the speed command is 600 r/min, the related fundamental ω is 80 π rad/s. Bode diagrams of the current closed loop transfer function with $k_{p2} = 1, 5, 10$, and $k_{i3} = 1, 10, 100$ are shown in Fig. 16, while k_{p3} and k_{i2} are invariant, thereby the influence of k_{p2} on sixth current harmonic and the influence of k_{i3} on 12th current harmonic are both investigated. It can be indicated that with the increase of k_{p2}, the gain of at the resonant frequency 6ω is decreased, thus, sixth current harmonic suppression effect is enhanced. However, with the increase of k_{i3}, the gain of current harmonic at the resonant frequency 12ω is

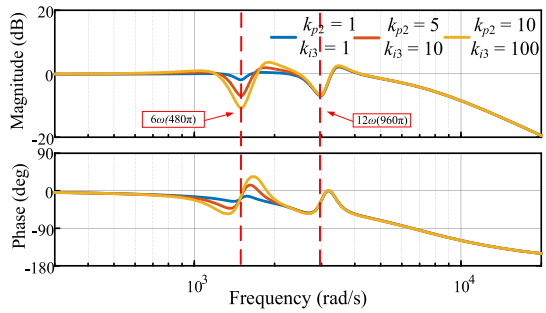

Fig. 16. Bode diagram with different k_{p2} and k_{i3}.

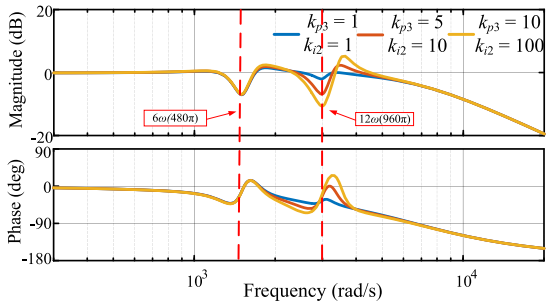

Fig. 17. Bode diagram with different k_{p3} and k_{i2}.

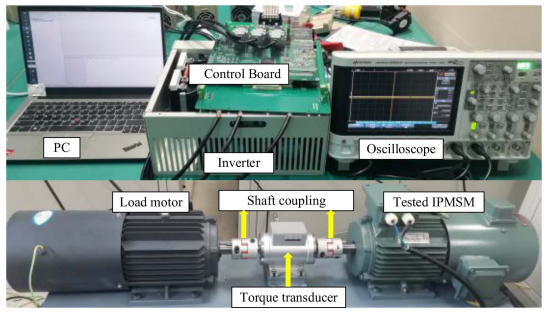

Fig. 18. Experimental platform of IPMSM drive system.

TABLE I
IPMSM PARAMETERS IN EXPERIMENT

Parameters	Value	Parameters	Value
Rated power P_N	17.26 kW	Stator resistance R_s	0.11 Ω
Rated voltage U_N	380 V	d-axis inductance L_d	3.686 mH
Rated current I_N	27.6 A	q-axis inductance L_q	4.072 mH
Rated speed ω_N	6500 r/min	Flux linkage ψ_f	0.1949 Wb
Rated torque T_N	26 N·m	Motor inertia J	0.0016 kg·m^2
Pole pairs p_n	2	DC bus voltage U_{dc}	537 V

invariant, which means that k_{i3} has no influence on 12th current harmonic suppression effect.

Bode diagrams of the current loop closed loop transfer function with k_{p3} = 1, 5, 10, and k_{i2} = 1, 10, 100 are shown in Fig. 17. The k_{p2} and k_{i3} are invariant, thereby the influence of k_{i2} on sixth current harmonic and the influence of k_{p3} on 12th current harmonic are both investigated. It can be indicated that with the increase of k_{p3}, the negative gain of current harmonic at the resonant frequency 12ω is increased, thus, 12th current harmonic suppression effect is enhanced. However, with the increase of k_{i2}, the gain of current harmonic at the resonant frequency 6ω is invariant, which means that k_{i2} has no influence on sixth current harmonic suppression effect.

V. EXPERIMENTAL RESULTS

The proposed scheme has been verified on the IPMSM experimental platform shown in Fig. 18. The main parameters of tested IPMSM are listed in Table I. The digital control unit is digital signal processor (DSP), type is TMS320F28335. The program is downloaded to DSP through computer. The inverter is used to drive the IPMSM, the carrier frequency of inverter is 10 kHz, and the dead time period is 5 μs. An oscilloscope is applied to display the current signals, and the sample rate is 25 kHz. The sampled signals data are imported into MATLAB for data processing.

In the compared methods, the proportionality coefficient m is the same, and it is 0.5. The filter coefficient k only exists in NF-SOGI, and it is 0.7. In the voltage compensation generation of two compared methods, PI parameters are the same. In details, $k_{p2} = 45$, $k_{i2} = 100$, $k_{p3} = 20$, and $k_{i3} = 100$.

A. Verification of Current Harmonics Convergence Effect

1) Target Current Harmonic: As one suppression target, the experimental results of sixth current harmonic are compared in Fig. 19. Speed command is 600 r/min, fundamental frequency is 40 Hz, and load torque is 10 N·m.

In Fig. 19(a) and (b), it shows the d-axis current waveform without current harmonics suppression and the FFT analysis, respectively. It can be seen that the fundamental current is dc signal in d-q synchronous rotating coordinate frame, while the current harmonics are ac signals. Through FFT analysis, the amplitude of sixth current harmonic is 5.99 dB, and that of 12th harmonic is −5.99 dB, so that d-axis current mainly contains 6th and 12th current harmonic, which is consistent with the theoretical analysis on harmonics model in Section II.

In Fig. 19(c) and (d), it shows the convergence effect of target sixth current harmonic based on SOGI. In Fig. 19(c), it can be seen that target sixth current harmonic is convergent with stable frequency. In Fig. 19(d), the convergence result of target sixth current harmonic is 5.95 dB, which is basically consistent with

$$G(s) = G_{PI1}(s)\frac{K_{pwm}}{(T_{pwm}s+1)(L_ds+R_s)+K_{pwm}[G_{PI2}(s)G_{\text{NF\_SOGI\_6}\omega}(s)+G_{PI3}(s)G_{\text{NF\_SOGI\_12}\omega}(s)]} \tag{29}$$

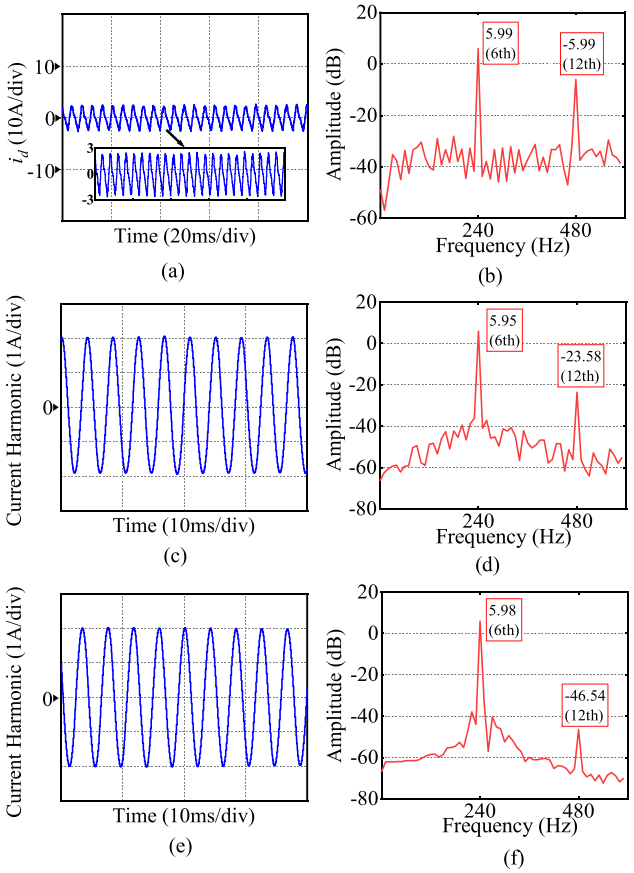

Fig. 19. Comparative experimental results of target sixth current harmonic convergence effect at 600 r/min and 10 N·m load torque. (a), (b) d-axis current and its FFT analysis without suppression method. (c), (d) Target sixth current harmonic from SOGI and its FFT analysis. (e), (f) Target sixth current harmonic from cross-decoupled NF-SOGI and its FFT analysis.

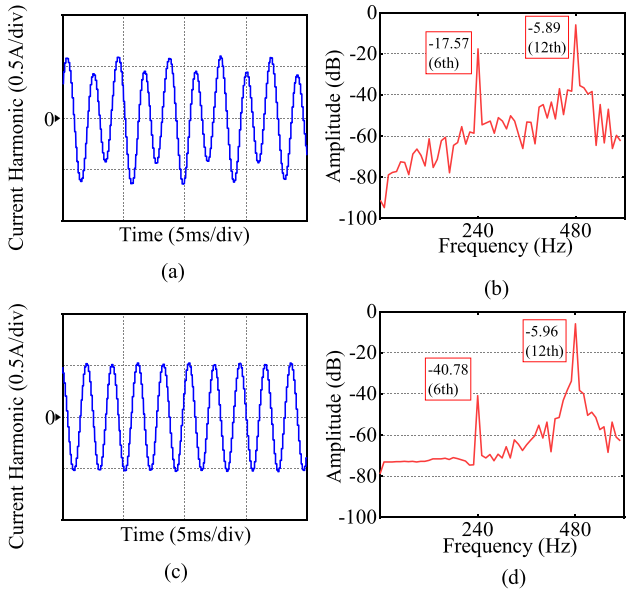

Fig. 20. Comparative experimental results of target 12th current harmonic convergence effect at 600 r/min and 10N·m load torque. (a), (b) Target 12th current harmonic from SOGI and its FFT analysis. (c), (d) Target 12th current harmonic from cross-decoupled NF-SOGI and its FFT analysis.

the actual amplitude 5.99 dB in Fig. 19(b), the amplitude of 12th current harmonic is reduced from −5.99 dB to −23.58 dB, and the amplitudes of other nontarget current harmonics are reduced below −40 dB. Therefore, the target sixth current harmonic can be reserved by SOGI, while the nontarget current harmonics are suppressed, and the experimental results are consistent with the analysis in Section III.

In Fig. 19(e) and (f), it shows the convergence effect of target sixth current harmonic based on cross-decoupled NF-SOGI. Compared Fig. 19(e) with (c), it can be indicated that the convergence effect of target sixth current harmonic is nearly the same with that of SOGI. However, compared Fig. 19(f) with (d), the convergence result of target sixth current harmonic is 5.98 dB, and thus, the convergence precision of NF-SOGI is closer to the actual value 5.99 dB than that of SOGI, and the amplitude of 12th current harmonic is further reduced from −23.58 dB to −46.54 dB, and the amplitudes of other nontarget current harmonics are also further reduced. Therefore, based on cross-decoupled NF-SOGI, the convergence effect of target sixth current harmonic is more precision than the typical SOGI, and the nontarget current harmonics are further suppressed. The experimental results are consistent with the analysis in Section IV-B.

As another suppression target, the experimental results of 12th current harmonic are compared in Fig. 20. Speed command is 600 r/min, fundamental frequency is 40 Hz, and load torque is 10 N·m.

In Fig. 20(a) and (b), it shows the convergence effect of target 12th current harmonic based on typical SOGI. It can be seen that the target 12th current harmonic is unstable convergence with obvious amplitude fluctuation, which is caused by sixth current harmonic. In details, the amplitude of sixth current harmonic is 0.133 A calculated from −17.57 dB, and 0.133 A is close to the amplitude of target 12th current harmonic, which is 0.501 A calculated from −5.89 dB. Therefore, the coupled issue is verified, that is nontarget current harmonic affects the convergence precision of target current harmonic.

In Fig. 20(c) and (d), it shows the convergence effect of target 12th current harmonic based on NF-SOGI. It can be seen that the convergence result of target 12th current harmonic is −5.96 dB and stable without the amplitude fluctuation, because the amplitude of sixth current harmonic is reduced from 0.133 A to 0.009 A calculated from −40.78 dB, so that sixth current harmonic has less influence on 12th current harmonic. Therefore, based on cross-decoupled NF-SOGI, the convergence precision of target 12th current harmonic is improved and closer to the actual amplitude −5.99 dB shown in Fig. 19(b), and thus all the nontarget current harmonics are also further reduced, so that the coupled issue is addressed in NF-SOGI. The experimental results are consistent with the analysis in Section IV-B.

In conclusion, through the target current harmonic based on NF-SOGI, the target current harmonic are decoupled with the nontarget current harmonics, so that the target current harmonics is not affected by the nontarget current harmonics. With the same parameter m to keep the same dynamic convergence response

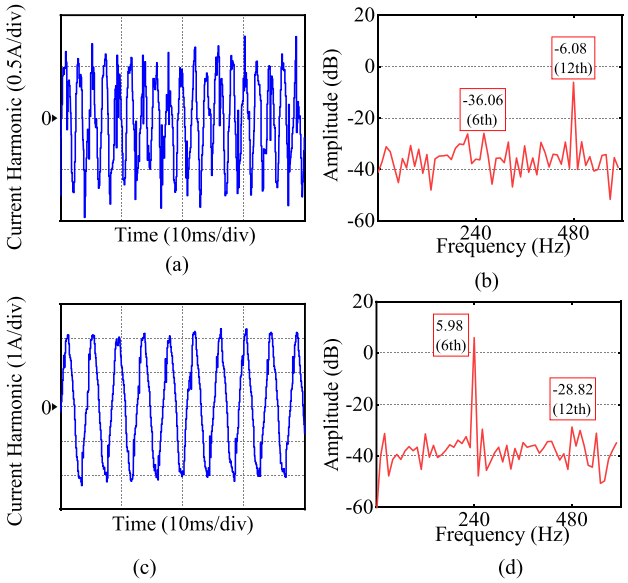

Fig. 21. Experimental results of nontarget current harmonic from NF-SOGI at 600 r/min and 10 N·m load torque. (a), (b) Nonsixth current harmonic and its FFT analysis. (c), (d) Non-12th current harmonic and its FFT analysis.

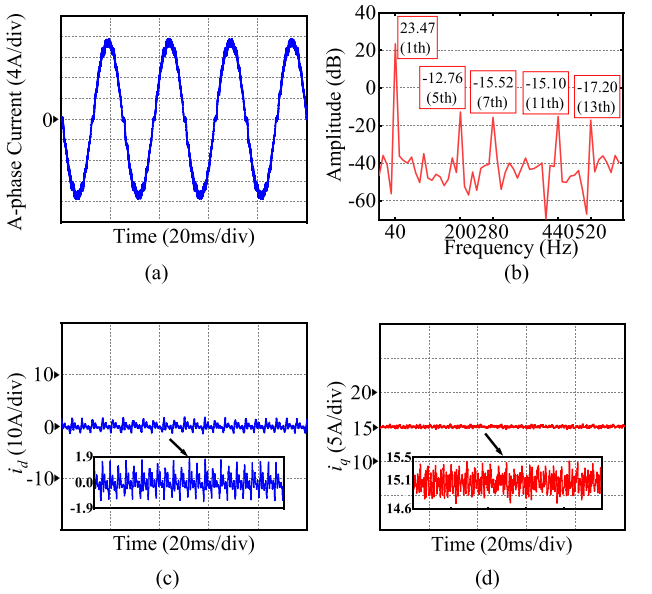

Fig. 22. Experimental results of current harmonics suppression method based on typical SOGI at 600 r/min and 10 N·m load torque. (a) A-phase current waveform. (b) FFT analysis. (c) *d*-axis current. (d) *q*-axis current.

with SOGI, the stable convergence precision of target current harmonics is enhanced, so that the tradeoff issue is addressed through parameter k in NF-SOGI.

2) Nontarget Current Harmonics: In the cross-decoupled NF-SOGI, the nontarget current harmonics are extracted and applied to address the coupled issue. Therefore, the nontarget current harmonics from NF-SOGI are verified in Fig. 21. Speed command is 600 r/min, fundamental frequency is 40 Hz, and load torque is 10 N·m.

In Fig. 21(a) and (b), it shows the nonsixth current harmonic and its FFT analysis. Through FFT analysis, it can be seen that the amplitude of sixth current harmonic is reduced from 5.99 dB to −36.06 dB in the nonsixth current harmonics, and the mainly component is 12th current harmonic, whose amplitude is −6.08 dB and is basically consistent with −5.99 dB in Fig. 19(b). In Fig. 21(c) and (d), it shows the non-12th current harmonic and its FFT analysis. It can be seen that the amplitude of 12th current harmonic is reduced from −5.99 dB to −28.82 dB in the non-12th current harmonics, and the mainly component is sixth current harmonic, whose amplitude is 5.98 dB and basically consistent with 5.99 dB in Fig. 19(b). Therefore, the attenuation effect on the nontarget current harmonics is enhanced, which indicates that the influence of target current harmonic on the convergence precision of nontarget current harmonic is reduced, so that the convergence precision of nontarget current harmonic is improved, and the coupled issue is addressed. The experimental results are consistent with the analysis in Section IV-B.

In summary, through the nontarget current harmonics based on NF-SOGI, the nontarget current harmonics are decoupled with the target current harmonics. Therefore, the nontarget current harmonics are also not affected by the target current harmonic, and thus the convergence precision of nontarget current harmonics is better. The parameter k improves the convergence precision of nontarget current harmonics and addresses the tradeoff issue in SOGI.

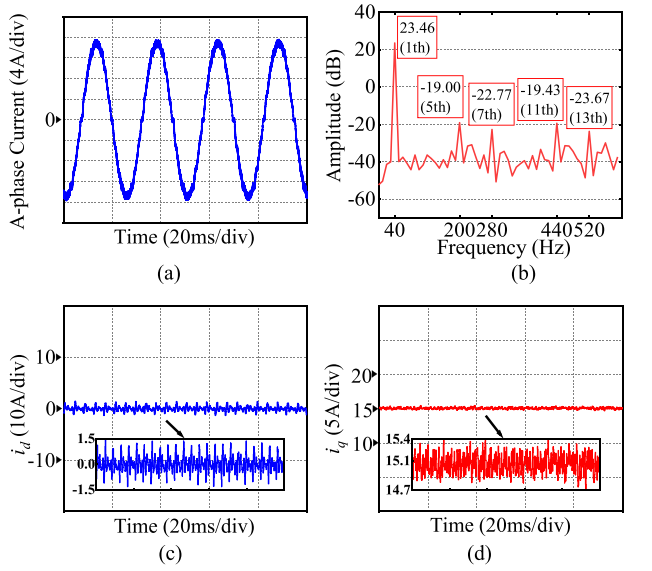

Fig. 23. Experimental results of current harmonics suppression method based on cross-decoupled NF-SOGI at 600 r/min and 10 N·m load torque. (a) A-phase current waveform. (b) FFT analysis. (c) *d*-axis current. (d) *q*-axis current.

B. Verification of Current Harmonics Suppression Effect

1) With the Same Load Torque: The current harmonics suppression effect between typical SOGI and NF-SOGI are compared in Figs. 22 and 23, respectively. Speed command is 600 r/min, the fundamental frequency is 40 Hz, and the load torque is 10 N·m.

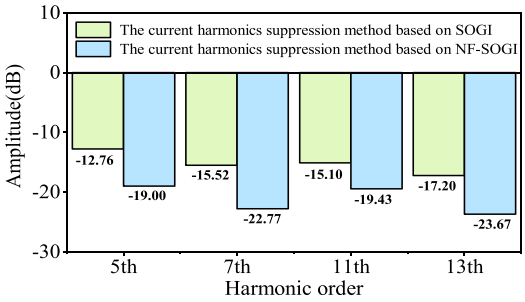

Fig. 24. Current harmonics contents comparison between typical SOGI and the cross-decoupled NF-SOGI.

Compared Figs. 22(a) and (b) with 23(a) and (b), it can be seen that the amplitude of fifth stator current harmonic is reduced from −12.76 dB to −19.00 dB, the amplitude of seventh stator current harmonic is reduced from −15.52 dB to −22.77 dB, the amplitude of 11th stator current harmonic is reduced from −15.10 dB to −19.43 dB, and the amplitude of 13th stator current harmonic is reduced from −17.20 dB to −23.67 dB. Therefore, the whole current harmonics suppression effect are further suppressed, so that the sine degree of the A-phase current waveform is improved based on the cross-decoupled NF-SOGI. In Fig. 22(c) and (d), it can be seen that i_d is fluctuant between −1.9 A and 1.9 A, and i_q is fluctuant between 14.6 A and 15.5 A. While in Fig. 23(c) and (d), i_d is fluctuant between −1.5 A and 1.5 A, and i_q is fluctuant between 14.7 A and 15.4 A. Therefore, the amplitude fluctuation of i_d and i_q gets narrower, and it indicates that the mainly current harmonics are further suppressed based on the cross-decoupled NF-SOGI. Compared typical SOGI with the cross-decoupled NF-SOGI, the amplitude of 5th, 7th, 11th, and 13th stator current harmonic in Figs. 22(b) and 23(b) are listed for intuitive comparison in Fig. 24.

In conclusion, the current harmonics suppression method based on cross-decoupled NF-SOGI is applied, 5th, 7th, 11th, and 13th stator current harmonics are further suppressed, and the fluctuation of i_d and i_q is reduced under steady state condition. Therefore, it can be indicated that a higher convergence precision of current harmonics contributes to a better suppression performance of current harmonics.

2) With the Different Load Torque: In IPMSM control system, with the growth of load torque, the amplitude of stator current is increased, so that it leads to increase the amplitude of all the current harmonics in (3), including the target current harmonic. Therefore, the current harmonic suppression effect based on cross-decoupled NF-SOGI is verified under the different load torques, which are 2 N·m in Fig. 25 and 26 N·m in Fig. 26, respectively. Speed command is 600 r/min, fundamental frequency is 40 Hz.

Compared Figs. 23 with 25 and 26, it can be seen that with the increase of load torque, the amplitude of stator current is increased, and the amplitude of all the current harmonics in (3) is increased as well, so that it results in the fluctuation of i_d and i_q. When the load torque is 2 N·m, 10 N·m, and 26 N·m, the fluctuation of i_d is between −0.6 A and 0.8 A, between −1.5 A and 1.5 A, between −2.2 A and 2.2 A, respectively. With the

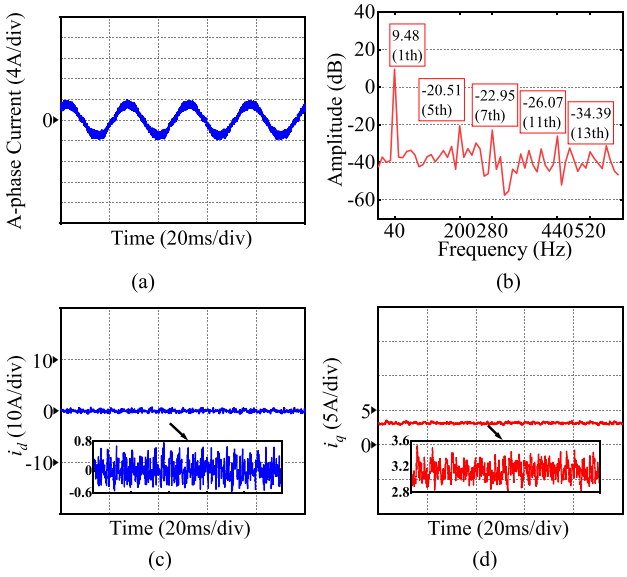

Fig. 25. Experimental results of current harmonics suppression method based on cross-decoupled NF-SOGI at 600 r/min and 2 N·m load torque. (a) A-phase current waveform. (b) FFT analysis. (c) *d*-axis current. (d) *q*-axis current.

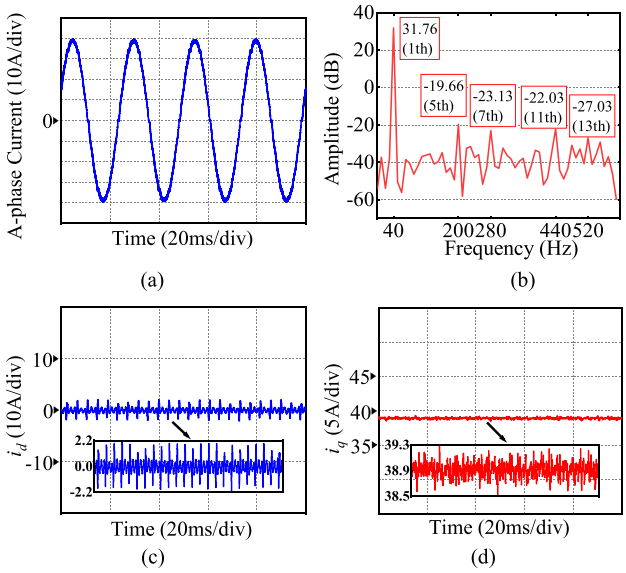

Fig. 26. Experimental results of current harmonics suppression method based on cross-decoupled NF-SOGI at 600 r/min and 26 N·m load torque. (a) A-phase current waveform. (b) FFT analysis. (c) *d*-axis current. (d) *q*-axis current.

growth of load torque, the fluctuation of i_d is increased. Since $i_d = 0$ is the control command, all the current harmonics can be clearly reflected by the amplitude fluctuation of i_d. It also proves that the amplitude of each current harmonics is increased with the growth of load torque. Same conclusion can be obtained by the fluctuation of i_q.

Under three different load torque, the amplitude of 5th, 7th, 11th, and 13th stator current harmonic shown in Figs. 23(b), 25(b) and 26(b) are listed for intuitive comparison in Fig. 27. Since the current harmonic suppression method based on cross-decoupled NF-SOGI is applied, although the increasing load

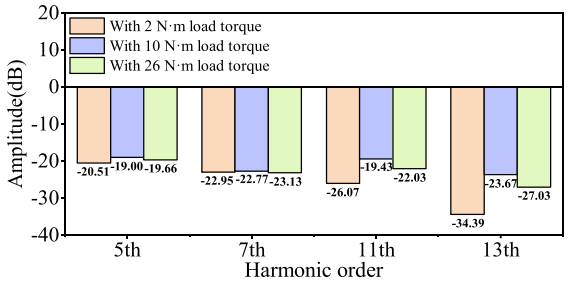

Fig. 27. Comparative experimental results of the proposed NF-SOGI with the different load torque.

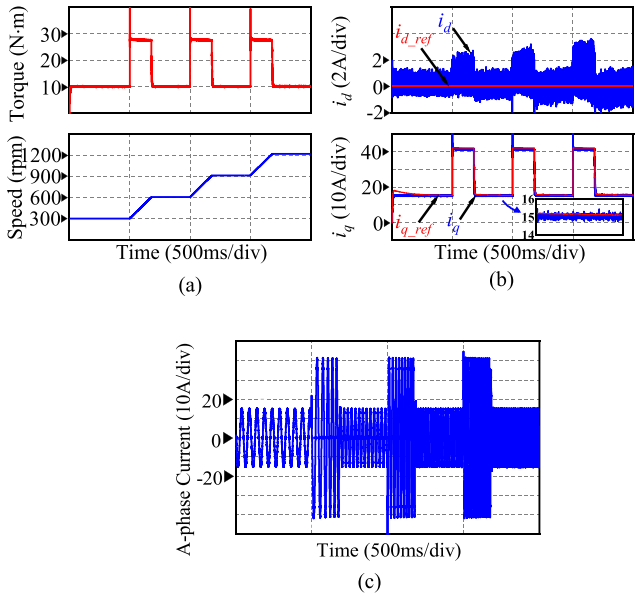

Fig. 28. Experimental waveforms during the step variation of speed command. (a) Speed and torque waveforms. (b) *dq*-axis current. (c) A-phase current waveform.

torque results in more current harmonics and the bigger fluctuation of i_d and i_q, the amplitude of 5th, 7th, 11th, and 13th stator current harmonic are effectively suppressed below -20 dB, and the corresponding peaks value of current harmonics can be calculated and are less than 0.1 A. (1 dB $=$ 20lg(M), M is the peaks value of current harmonic.) Compared with the fundamental current in Figs. 23(a), 25(a), and 26(a), as an effective suppression result, 0.1 A is rather small and can be ignored.

In conclusion, with the growth of load torque, the amplitude of current harmonics is increased, and results in the fluctuation of i_d and i_q. When the current harmonics suppression method based on cross-decoupled NF-SOGI is applied, the fluctuation of i_d and i_q can be reduced, because 5th, 7th, 11th, and 13th stator current harmonics can be effectively suppressed.

C. Verification of the Dynamic Process

1) Dynamic Performance of NF-SOGI: Fig. 28 shows the experimental waveforms of the proposed method during the step variation in motor speed. The torque command is 10 N·m, and

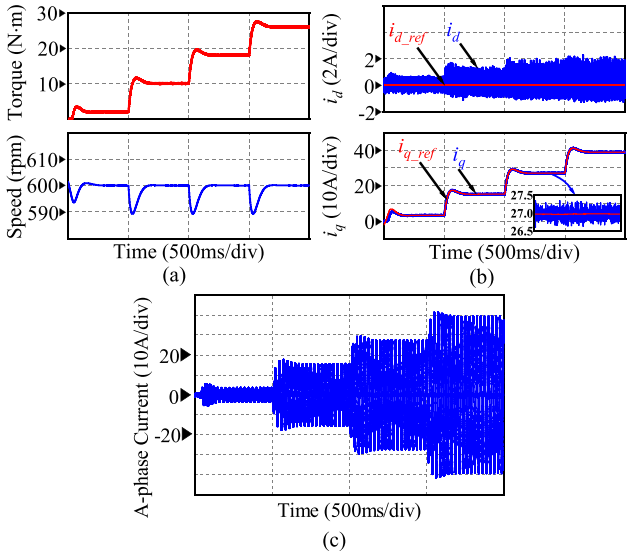

Fig. 29. Experimental waveforms during the step variation of load torque. (a) Speed and torque waveforms (b) *dq*-axis current. (c) A-phase current waveform.

the motor speed is step changed from 300 r/min to 600 r/min, to 900 r/min, to 1200 r/min eventually. When the motor speed command is step changed, i_d and i_q have a better dynamic response characteristic and reach the steady state quickly. It indicates that the parameters designed at 600 r/min are still applicable at other speed commands.

Fig. 29 shows the experimental waveforms of the proposed method during changes in torque load. The speed command is 600 r/min, and the load torque is step changed from 2 N·m to 10 N·m, to 18 N·m, to 26 N·m eventually. It can be seen that a good steady-state and dynamic performance can be obtained during the step torque load. During the load torque is step changed, i_d and i_q have a better dynamic response characteristic and reach the steady state quickly. With the increasing of torque load, the fundamental current is increased, and the current harmonics in i_d are increased, but i_d current fluctuation is suppressed within -2 A and 2 A.

2) Dynamic Comparison Between PR and NF-SOGI: The experimental comparison results between NF-SOGI and PR are shown in Fig. 30. The experimental speed command is 600 r/min, and the step load torque is increased from 10 N·m to 18 N·m. In Fig. 30(a), i_d is fluctuant between -2 A and 2 A before step load, and between -3 A and 3 A after step load. In Fig. 30(b), i_q is fluctuant between 14.5 A and 15.5 A before step load, and between 26.5 A and 27.5 A after step load. While in Fig. 30(c) and (d), i_d is fluctuant between -1.5 A and 1.5 A before step load, and between -2.5 A and 2.5 A after step load. i_q is fluctuant between 14.8 A and 15.2 A before step load, and between 26.8 A and 27.2 A after step load.

Compared with the method based on PR, the fluctuation range of i_d and i_q gets narrower based on NF-SOGI before and after step load. The cut-off frequency ω_c of PR controller is associated with the dynamic and stable performance, and the increasing of ω_c improves the bandwidth and accelerates the response speed, although ω_c does not affect the gain at the resonant frequency

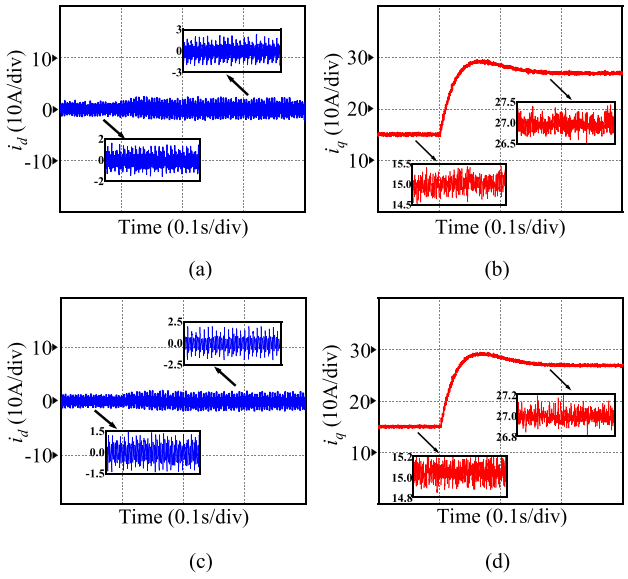

Fig. 30. Experimental comparison results between the current harmonics suppression method based on the cross-decoupled NF-SOGI and the current harmonics suppression method based on PR. (a), (b) *d*-axis and *q*-axis current waveforms based on PR, (c), (d) *d*-axis and *q*-axis current waveforms based on the cross-decoupled NF-SOGI.

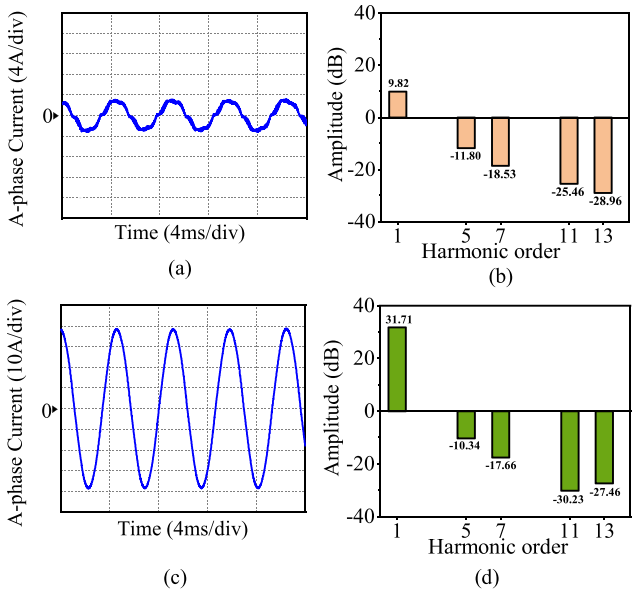

Fig. 31. Experimental results of current harmonics suppression method based on cross-decoupled NF-SOGI at 6500 r/min with 2 N·m and 26 N·m load torque. (a) Stator current with light load. (b) FFT analysis with light load. (c) Stator current with rated load. (d) FFT analysis with rated load.

point, but it introduces high-frequency noise, especially for the suppression of high-frequency current harmonics. This issue is carefully considered and optimized for design NF-SOGI. Therefore, it achieves a better suppression effects of current harmonics in NF-SOGI.

3) Verification of High-Speed Operation Performance: Based on proposed cross-decoupled NF-SOGI method, the experimental results of the current harmonics suppression method at rated speed 6500 r/min have been verified in Fig. 31, and the fundamental frequency is 210 Hz. In Fig. 31(a) and (b), it shows the current harmonics suppression effect at 6500 r/min and 2 N·m, the amplitude of 5th, 7th, 11th, and 13th stator current harmonics are −11.80 dB, −18.53 dB, −25.46 dB, and −28.96 dB, respectively. In Fig. 31(c) and (d), it shows the current harmonics suppression effect at 6500 r/min and 26 N·m, the amplitude of 5th, 7th, 11th, and 13th stator current harmonics are −10.34 dB, −17.66 dB, −30.23 dB, and −27.46 dB, respectively.

As the phase inductance value of high-speed PMSM is rather small, the motor is more sensitive to the variation of current and voltage, and it results in a larger current ripple, which contents much more current harmonics at high-speed. Therefore, compared with the experimental results at low-speed 600 r/min and same load 2 N·m in Fig. 25, although more current harmonics exists at high-speed than at low-speed, the amplitudes of current harmonics are nearly the same. Meanwhile, compared Fig. 31(a) and (c), the sine degree of stator current is improved with the increase of load, only the amplitude of fundamental current is increased, but the amplitudes of current harmonics are not increased. From the above two aspects, the proposed method is effective to suppress the current harmonics at high-speed and at low-speed.

VI. Conclusion

In this article, a current harmonics suppression method based on cross-decoupled NF-SOGI is proposed to improve the suppression effect of current harmonic in IPMSM control system. In the proposed NF-SOGI, utilizing the opposite characteristics of SOGI and NF in the same central frequency, SOGI is applied to extract the target current harmonic, while NF is applied to extract the nontarget current harmonics, and thus, the current harmonics are decoupled. Through the cross-link between SOGI and NF, the proposed NF-SOGI is reconstructed as double-degree of freedom, and thus, both the stable convergence precision and the dynamic convergence performance can be improved at the same time. Therefore, more precise convergence of target current harmonic leads to a better suppression performance. The experimental results illustrate that the proposed scheme can improve the suppression effect of current harmonics.

As a perspective, the current harmonics suppression is vital in many industrial applications, and its effect is affected by many factors, such as the variation of motor parameters, current sample error, and discretization of controller. These factors affect the voltage compensation. More research can be explored to further improve the current harmonics suppression effect.

References

[1] K. Rajashekara, "Present status and future trends in electric vehicle propulsion technologies," *IEEE J. Emerg. Sel. Topics Power Electron.*, vol. 1, no. 1, pp. 3–10, Mar. 2013.

[2] W. Liang, P. C.-K. Luk, and W. Fei, "Investigation of magnetic field interharmonics and sideband vibration in the FSCW IPMSM drive with the SPWM technique," *IEEE Trans. Power Electron.*, vol. 33, no. 4, pp. 3315–3324, Apr. 2018.

[3] X. Ding, J. Cheng, Z. Zhao, and P. C. K. Luk, "A high-precision and high-efficiency PMSM driver based on power amplifiers and RTSPSs," *IEEE Trans. Power Electron.*, vol. 36, no. 9, pp. 10470–10480, Sep. 2021.

[4] J. Liu and Y. Zhang, "Current pulsation suppression method based on power current closed-loop control for a PMSM under fluctuating DC-link voltage," *IEEE Trans. Power Electron.*, vol. 37, no. 1, pp. 761–770, Jan. 2022.
[5] S. Wang, J. Kang, M. Degano, A. Galassini, and C. Gerada, "An accurate wide-speed range control method of IPMSM considering resistive voltage drop and magnetic saturation," *IEEE Trans. Ind. Electron.*, vol. 67, no. 4, pp. 2630–2641, Apr. 2020.
[6] C. Lai, G. Feng, K. Mukherjee, V. Loukanov, and N. C. Kar, "Torque ripple modeling and minimization for interior PMSM considering magnetic saturation," *IEEE Trans. Power Electron.*, vol. 33, no. 3, pp. 2417–2429, Mar. 2018.
[7] H. Fang, D. Li, R. Qu, and P. Yan, "Modulation effect of slotted structure on vibration response in electrical machines," *IEEE Trans. Ind. Electron.*, vol. 66, no. 4, pp. 2998–3007, Apr. 2019.
[8] M. Yang, X. Lang, J. Long, and D. Xu, "Flux immunity robust predictive current control with incremental model and extended state observer for PMSM drive," *IEEE Trans. Power Electron.*, vol. 32, no. 12, pp. 9267–9279, Dec. 2017.
[9] F. Yang et al., "Complex coefficient active disturbance rejection controller for current harmonics suppression of IPMSM drives," *IEEE Trans. Power Electron.*, vol. 37, no. 9, pp. 10443–10454, Sep. 2022.
[10] G. Feng, C. Lai, M. Kelly, and N. C. Kar, "Dual three-phase PMSM torque modeling and maximum torque per peak current control through optimized harmonic current injection," *IEEE Trans. Ind. Electron.*, vol. 66, no. 5, pp. 3356–3368, May 2019.
[11] M. Gu, Z. Wang, and B. Wang, "Optimization of torque ripple for low-carrier-ratio dual three-phase PMSM with pulse pattern control," *IEEE Trans. Power Electron.*, vol. 38, no. 12, pp. 15091–15096, Dec. 2023.
[12] D. Flieller, N. K. Nguyen, P. Wira, G. Sturtzer, D. O. Abdeslam, and J. Mercklé, "A self-learning solution for torque ripple reduction for nonsinusoidal permanent-magnet motor drives based on artificial neural networks," *IEEE Trans. Ind. Electron.*, vol. 61, no. 2, pp. 655–666, Feb. 2014.
[13] Z. Wu, Z. Yang, K. Ding, and G. He, "Transfer mechanism analysis of injected voltage harmonic and its effect on current harmonic regulation in FOC PMSM," *IEEE Trans. Power Electron.*, vol. 37, no. 1, pp. 820–829, Jan. 2022.
[14] M. Tian, B. Wang, Y. Yu, Q. Dong, and D. Xu, "Discrete-time repetitive control-based ADRC for current loop disturbances suppression of PMSM drives," *IEEE Trans. Ind. Inform.*, vol. 18, no. 5, pp. 3138–3149, May 2022.
[15] B. Wang, M. Tian, Y. Yu, Q. Dong, and D. Xu, "Enhanced ADRC with quasi-resonant control for PMSM speed regulation considering aperiodic and periodic disturbances," *IEEE Trans. Transp. Electrific.*, vol. 8, no. 3, pp. 3568–3577, Sep. 2022.
[16] M. Tian, B. Wang, Y. Yu, Q. Dong, and D. Xu, "Adaptive active disturbance rejection control for uncertain current ripples suppression of PMSM drives," *IEEE Trans. Ind. Electron.*, vol. 71, no. 3, pp. 2320–2331, Mar. 2024.
[17] W. Wang, C. Liu, S. Liu, Z. Song, H. Zhao, and B. Dai, "Current harmonic suppression for permanent-magnet synchronous motor based on Chebyshev filter and PI controller," *IEEE Trans. Magn.*, vol. 57, no. 2, Feb. 2021, Art. no. 8201406.
[18] P. L. Chapman and S. D. Sudhoff, "A multiple reference frame synchronous estimator/regulator," *IEEE Trans. Energy Convers.*, vol. 15, no. 2, pp. 197–202, Jun. 2000.
[19] L. Yan et al., "Multiple synchronous reference frame current harmonic regulation of dual three phase PMSM with enhanced dynamic performance and system stability," *IEEE Trans. Ind. Electron.*, vol. 69, no. 9, pp. 8825–8838, Sep. 2022.
[20] H. Dhulipati, S. Mukundan, C. Lai, K. Mukherjee, J. Tjong, and N. C. Kar, "Multiple reference frame-based extended concentrated wound PMSM model considering PM flux linkage and inductance harmonics," *IEEE Trans. Energy Convers.*, vol. 34, no. 2, pp. 731–740, Jun. 2019.
[21] Y. Bai et al., "An adaptive-frequency harmonic suppression strategy based on vector reconstruction for current measurement error of PMSM drives," *IEEE Trans. Power Electron.*, vol. 38, no. 1, pp. 34–40, Jan. 2023.
[22] J. Qu, J. Jatskevich, C. Zhang, and S. Zhang, "Torque ripple reduction method for permanent magnet synchronous machine drives with novel harmonic current control," *IEEE Trans. Energy Convers.*, vol. 36, no. 3, pp. 2502–2513, Sep. 2021.
[23] L. Wang, Z. Q. Zhu, H. Bin, and L. M. Gong, "Current harmonics suppression strategy for PMSM with non-sinusoidal back-EMF based on adaptive linear neuron method," *IEEE Trans. Ind. Electron.*, vol. 67, no. 11, pp. 9164–9173, Nov. 2020.
[24] Q. Zhang, Y. Fan, J. Chen, C. Yang, and M. Cheng, "A current harmonic suppression method for PMSM based on harmonic prediction adaptive notch filter," *IEEE Trans. Energy Convers.*, vol. 37, no. 3, pp. 2107–2118, Sep. 2022.
[25] P. Rodriguez, A. Luna, R. S. Munoz-Aguilar, I. Etxeberria-Otadui, R. Teodorescu, and F. Blaabjerg, "A stationary reference frame grid synchronization system for three-phase grid-connected power converters under adverse grid conditions," *IEEE Trans. Power Electron.*, vol. 27, no. 1, pp. 99–112, Jan. 2012.
[26] F. Muzi and M. Barbati, "A real-time harmonic monitoring aimed at improving smart grid power quality," in *Proc. IEEE Int. Conf. Smart Meas. Future Grids*, 2011, pp. 95–100.
[27] Q. Zhang et al., "A novel error-injected solution for compensation of current measurement errors in PMSM drive," *IEEE Trans. Ind. Electron.*, vol. 70, no. 5, pp. 4608–4619, May 2023.
[28] R. Zhao, Z. Xin, P. C. Loh, and F. Blaabjerg, "A novel flux estimator based on multiple second-order generalized integrators and frequency-locked loop for induction motor drives," *IEEE Trans. Power Electron.*, vol. 32, no. 8, pp. 6286–6296, Aug. 2017.
[29] W. Xu, Y. Jiang, C. Mu, and F. Blaabjerg, "Improved nonlinear flux observer-based second-order SOIFO for PMSM sensorless control," *IEEE Trans. Power Electron.*, vol. 34, no. 1, pp. 565–579, Jan. 2019.
[30] S. Wang et al., "Flux observer based on enhanced second-order generalized integrator with limit cycle oscillator for sensorless PMSM drives," *IEEE Trans. Power Electron.*, vol. 38, no. 12, pp. 15982–15995, Dec. 2023.
[31] G. Wang et al., "Enhanced position observer using second-order generalized integrator for sensorless interior permanent magnet synchronous motor drives," *IEEE Trans. Energy Convers.*, vol. 29, no. 2, pp. 486–495, Jun. 2014.
[32] Z. Xin, R. Zhao, F. Blaabjerg, L. Zhang, and P. C. Loh, "An improved flux observer for field-oriented control of induction motors based on dual second-order generalized integrator frequency-locked loop," *IEEE J. Emerg. Sel. Topics Power Electron.*, vol. 5, no. 1, pp. 513–525, Mar. 2017.

Chao Du (Member, IEEE) was born in Shannxi, China, in 1991. He received the B.S., M.S., and Ph.D. degrees in electrical engineering from the Xi'an University of Technology, Xi'an, China, in 2013, 2016, and 2020, respectively.

Since 2021, he has been a Postdoctor with the College of Electrical Engineering, Zhejiang University, where he is working on traction drive control of electric locomotives. His research interest includes the optimization control of ac drive systems.

Shuang Yang was born in Chengdu, China, in 1999. He received the B.S. degree in electrical engineering and automatization from the Chengdu University of Technology, Chengdu, China, in 2021. He is currently working toward the M.S. degree in electrical engineering with the Shaanxi University of Science and Technology, Xi'an, China.

His current research focuses on the control of electrical machines.

Lin Qiu (Senior Member, IEEE) received the B.S. and Ph.D. degrees in electrical engineering from the Department of Electrical Engineering, Tsinghua University, Beijing, China, in 2011 and 2017, respectively.

He is currently a Research Professor with the Zhejiang University, Hangzhou, China, with the University of Ilinois at Urbana-Champaign Institute, Zhejiang, China, and also with the College of Electrical Engineering, Zhejiang University, Hangzhou. His current research interests include transportation electrification, grid resilience enhancement, and data-driven system control algorithm.

Jien Ma (Member, IEEE) received the Ph.D. degree in mechatronics from Zhejiang University, Hangzhou, China, in 2009.

She is a Professor with the College of Electrical Engineering, Zhejiang University, where she is working on electrical machines and drives. Her research interests include the PM machines, core loss estimation, and reliability.

Youtong Fang (Senior Member, IEEE) received the B.S. and Ph.D. degrees in electrical engineering from the Hebei University of Technology, Tianjin, China, in 1984 and 2001, respectively.

He is currently a Professor with the College of Electrical Engineering, Zhejiang University, Hangzhou, China and State Key Laboratory of Fluid Power and Mechatronic Systems, Hangzhou. His research interests include application, control, and design of electrical machines.

Jose Rodriguez (Life Fellow, IEEE) received the Engineer degree in electrical engineering from the Universidad Tecnica Federico Santa Maria, Valparaiso, Chile, in 1977, and the Dr.-Ing. degree in electrical engineering from the University of Erlangen, Erlangen, Germany, in 1985.

Since 1977, he has been with the Department of Electronics Engineering, Universidad Tecnica Federico Santa Maria, where he was a Full Professor and President. From 2015 to 2019, he was the President with Universidad Andres Bello, Santiago, Chile. From 2022 to 2023, he was the President of Universidad San Sebastian, Santiago, Chile. He is the Director of the Center for Energy Transition, Universidad San Sebastian. He has coauthored two books, several book chapters, and more than 900 journal and conference papers. His research interests include multilevel inverters, new converter topologies, control of power converters, and adjustable-speed drives.

Dr. Rodriguez was the recipient of the number of best paper awards from journals of the IEEE, the National Award of Applied Sciences and Technology from the government of Chile in 2014, and the Eugene Mittelmann Award from the Industrial Electronics Society of the IEEE in 2015. He is Member of the Chilean Academy of Engineering. From 2014 to 2023, he was included in the list of Highly Cited Researchers published by Web of Science.